

Molecular Dynamics Simulation and Pulsed-Field Gradient NMR Studies of Bis(fluorosulfonyl)imide (FSI) and Bis[(trifluoromethyl)sulfonyl]imide (TFSI)-Based Ionic Liquids

Oleg Borodin,^{*,†,‡} W. Gorecki,[§] Grant D. Smith,[‡] and Michel Armand^{||}

Wasatch Molecular Inc., 2141 St. Marys Drive, Suite 102, Salt Lake City, Utah 84108, Department of Materials Science & Engineering, 122 South Central Campus Drive, Room 304, University of Utah, Salt Lake City, Utah 84112-0560, Laboratoire de Spectrométrie Physique, Université Joseph Fourier, Grenoble I-38401, BP 87, 38402 St. Martin D'hères Cedex, France, and Laboratoire de Réactivité et de Chimie des Solides, Université de Picardie Jules Verne, 33 rue Saint leu, 80039 Amiens Cedex, France

Received: December 17, 2009; Revised Manuscript Received: April 13, 2010

The pulsed-field-gradient spin-echo NMR measurements have been performed on 1-ethyl-3-methylimidazolium bis(fluorosulfonyl)imide ([emim][FSI]) and 1-ethyl-3-methylimidazolium [bis(trifluoromethyl)sulfonyl]imide ([emim][TFSI]) over a wide temperature range from 233 to 400 K. Molecular dynamics (MD) simulations have been performed on [emim][FSI], [emim][TFSI], [*N*-methyl-*N*-propylpyrrolidinium][FSI] ([pyr₁₃][FSI]), and [pyr₁₃][TFSI] utilizing a many-body polarizable force field. An excellent agreement between the ion self-diffusion coefficients from MD simulations and pfg-NMR experiments has been observed for [emim][FSI] and [emim][TFSI] ILs. The structure factor of [pyr₁₃][FSI], [pyr₁₄][TFSI], and [emim][TFSI] agreed well with the previously reported X-ray diffraction data performed by Umebayashi group. Ion packing in the liquid state is compared with packing in the corresponding ionic crystal. Faster transport found in the FSI-based ILs compared to that in TFSI-based ILs is associated with the smaller size of FSI[−] anion and lower cation–anion binding energies. A significant artificial increase of the barriers (by 3 kcal/mol) for the FSI[−] anion conformational transitions did not result in slowing down of ion transport, indicating that the ion dynamics is insensitive to the FSI[−] anion torsional energetic, while the same increase of the TFSI[−] anion barriers in [emim][TFSI] and [pyr₁₃][TFSI] ILs resulted in slowing down of the cation and anion transport by 40–50%. Details of ion rotational and translational motion, coupling of the rotational and translational relaxation are also discussed.

I. Introduction

Room temperature ionic liquids (ILs) have been widely investigated for use in lithium batteries,^{1–4} supercapacitors,^{5–10} dye-sensitized solar cells,¹¹ biphasic systems for separation and solvents for synthetic and catalytic applications,¹² and actuators¹³ and as a reaction media¹⁴ due to their outstanding properties that include negligible vapor pressure, excellent thermal and electrochemical stability, good dissolution properties with many organic and inorganic compounds, and low flammability. Improved IL performance for these and other applications can be achieved by tuning the combination of cations and anions to obtain the desired thermodynamic, solvating, and transport properties, as well as safety characteristics. For example, it has been observed that higher charge delocalization^{15,16} and small ion size¹⁷ often reduces viscosity and improves ion transport, while the length and nature of substituent groups on IL cations greatly affect the IL melting temperature (T_m), glass transition temperature (T_g), and thermal stability. The heat of vaporization, ion sizes, and cation–anion binding energies also influence ion transport.¹⁸

The use and performance of ILs for many applications is limited by their transport properties and molecular dynamics,

which are typically slow compared to those of nonionic organic solvents. Hence, there is much effort to develop new ILs that maintain their useful properties but exhibit significantly lower viscosity and increased ionic mobility. Recently, considerable attention has been focused on ILs based on the bis(fluorosulfonyl)imide, or FSI, anion, illustrated in Figure 1a, combined with 1-alkyl-3-methylimidazolium ($C_n\text{mim}^+$) and *N*-alkyl-*N*-methylpyrrolidinium (pyr_{1R}^+) cations, due to low viscosity, high conductivity, and acceptable electrochemical stability.^{19–23} Compared to extensively investigated bis(trifluoromethyl)sulfonyl]imide (TFSI or tf₂N, Figure 1b) ILs, FSI analogs exhibit significantly reduced viscosity and increased conductivity at room temperature.^{18,19,22,24} The specific choice of an IL for applications is dictated by compromise between its electrochemical stability, conductivity, melting point, and cost. For example, the pyr₁₃⁺ cation has a wide electrochemical window indicating electrochemical stability better than that of ILs with $C_n\text{mim}^+$,^{19,25–28} while emim⁺-containing ILs have higher ionic conductivity and lower viscosity than pyr₁₃-based analogs.¹⁹ Analysis of the melting temperatures of [pyr_{1R}][TFSI]²⁹ $R = 1, 2, 3$ and [$C_n\text{mim}$][TFSI]¹⁷ for $n = 1, 2, 3, 4, 6$ ILs as a function of the alkyl tail length has revealed that their melting points decrease with an initial increase of the alkyl tail for $R = 1–3$ and $n = 1–4$. However, longer tails result in undesirable slower ion dynamics and reduce the volume fraction of ionic groups.^{17,29} Often emim⁺ and pyr₁₃⁺ are chosen from the family of $C_n\text{mim}^+$

* Corresponding author. E-mail: Oleg.Borodin@utah.edu.

† Wasatch Molecular Inc.

‡ University of Utah.

§ Université Joseph Fourier.

|| Université de Picardie Jules Verne.

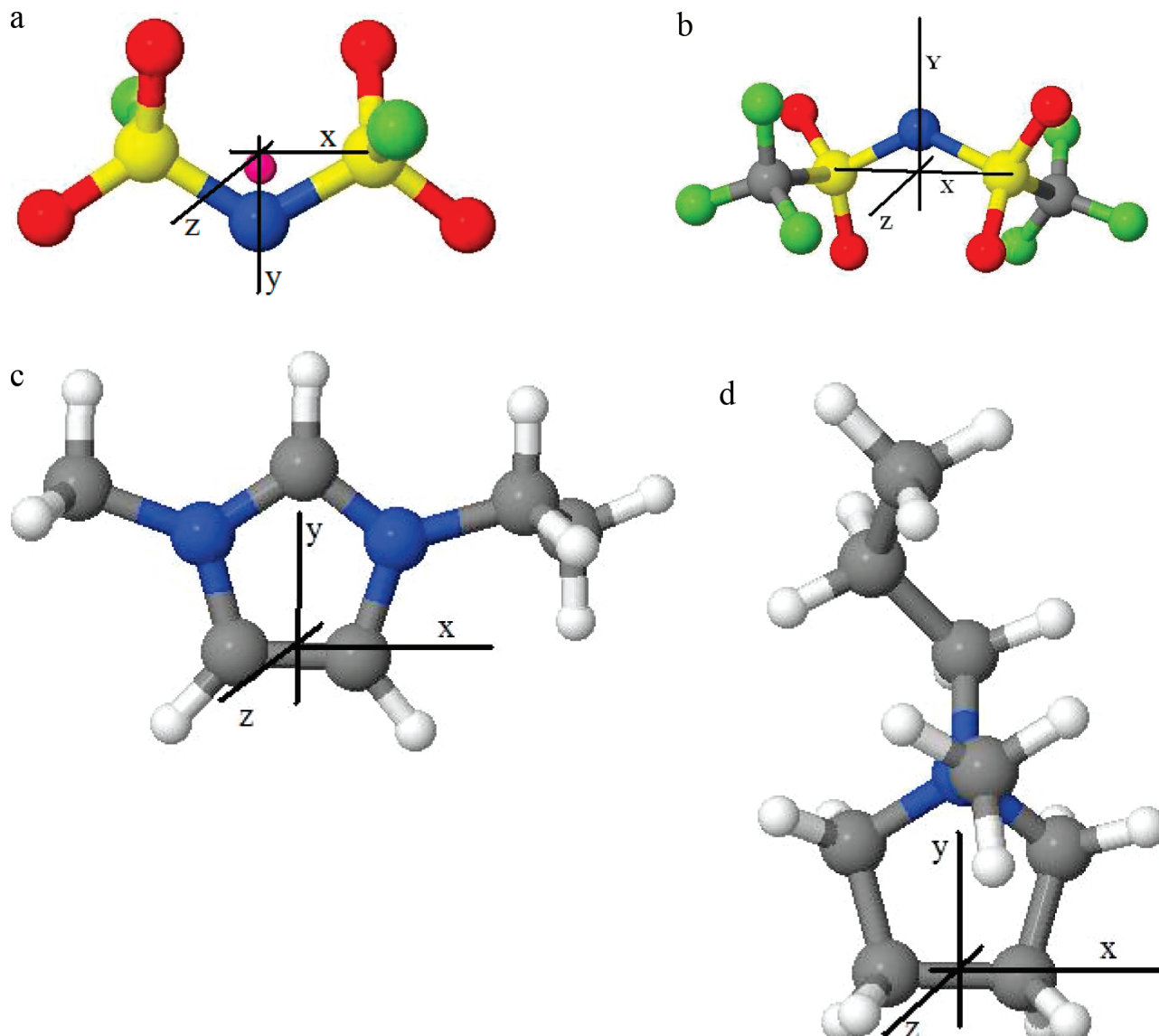


Figure 1. Simulated (a) bis(fluorosulfonyl)imide (FSI^-) and (b) bis[(trifluoromethyl)sulfonyl]imide (TFSI^-) anions and (c) 1-methyl-3-ethylimidazolium (emim^+) and (d) N -methyl- N -propylpyrrolidinium (pyr_{13}^+) cations. The coordinate basis for calculation of the rotational relaxation function are shown.

and pyr_{13}^+ cations as representing a good compromise between low melting point (below room temperature) and fast transport.

In 2006, we reported ion packing and transport from molecular dynamics (MD) simulations of $[\text{pyr}_{13}][\text{TFSI}]$ IL and $[\text{pyr}_{13}][\text{TFSI}]$ doped with LiTFSI salt.^{30,31} Recently, we have significantly extended that work and developed a transferable quantum chemistry-based transferable polarizable force field that allowed us to obtain from MD simulations accurate predictions of density, heat of vaporization, ion self-diffusion coefficients, conductivity, and viscosity for a wide range of ILs^{32–35} and EC: DMC/LiPF₆ liquid electrolyte.³⁶ Unlike previous efforts by Padua, Canongia Lopes,^{37–50} Maginn,^{51–60} and other groups,^{61–66} we included many-body polarization in the force field and made consistent efforts in constructing IL force fields that would be applicable beyond a few compounds of interest. While Yan et al.⁶⁷ and Chang et al.⁶⁸ reported MD simulations of $[\text{bmim}][\text{NO}_3]$ and dmim^+ with Cl^- , Br^- , and I^- using polarizable force fields, it is not clear if those force fields are transferable. Canongia Lopes and Padua developed force fields for ILs that covered a broad set of cations and anions.^{37–50} While the number of ILs included in the force field reported by Canongia Lopes and

Padua is impressive and IL density and crystal phase cell parameters are well reproduced, the ability of this force field to predict heat of vaporization and transport properties is much less so. For example, the enthalpy of vaporization for $[\text{C}_n\text{mim}][\text{TFSI}]$ was found to be approximately 20–40 kJ/mol higher⁶⁹ than values obtained from three independent experimental measurements.⁶¹ The self-diffusion coefficients obtained from simulations using Padua's force field were a factor of 5 smaller than experimental values for $[\text{emim}][\text{TFSI}]$.⁶¹ A sluggish transport has been found by in simulations by Picálek et al.⁷⁰ of $[\text{emim}][\text{PF}_6]$, $[\text{bmim}][\text{PF}_6]$, and $[\text{bmim}][\text{BF}_4]$ and by Tsuzuki et al.⁶⁴ for 13 ILs, while a number of other nonpolarizable force fields^{61,65,71–74} predicted ion transport in good agreement with experiments.

In this manuscript we further validate the ability of our recently developed polarizable force field to accurately predict ion transport by comparing simulation predictions to result of pfg-NMR experiments reported in this contribution for $[\text{emim}][\text{FSI}]$ and $[\text{emim}][\text{TFSI}]$. The pfg-NMR experiments reported here for $[\text{emim}][\text{TFSI}]$ extend the range of the previously reported¹⁷ data for this IL to the lower temperature. We compare

the structure factor with the recent X-ray data reported by the Umebayashi group.^{23,63,75} The validated simulations will be used to answer a number of questions about [emim][TFSI], [emim][FSI], [pyr₁₃][TFSI], and [pyr₁₃][FSI] ILs, such as (a) how different is the TFSI⁻ anion packing around cations from the FSI⁻ anion packing, (b) why do pyr₁₃⁺ and TFSI-based ILs have slower transport in comparison with ILs containing emim⁺ cation and FSI⁻ anion, and (c) is conformational relaxation of TFSI⁻ and FSI⁻ coupled to ion translational and rotational dynamics? Furthermore, we will discuss in detail ion rotational and translational motion, as well as anisotropy of rotational dynamics. The conformational equilibrium of the TFSI⁻ and FSI⁻ anion in the gas phase will be compared to that in the liquid phase from our simulations and Raman experiments.^{23,76-78}

The paper is organized as follows. In section II, pulsed-field gradient spin echo NMR (pfg-NMR) results are reported focusing on comparison between the temperature dependence of the ion self-diffusion coefficients in [emim][FSI] and [emim][TFSI]. MD simulation methodology and the force field used in our simulations are briefly described in section III. Results of MD simulations describing thermodynamic, transport and structural properties of [emim][FSI], [pyr₁₃][FSI], [emim][TFSI], and [pyr₁₃][TFSI] are reported in section IV.

II. Pulsed-Field Gradient NMR Measurements

Materials preparation: LiTFSI was used as received from 3 M. KFSI was a special order to Morita and was made according to the reaction



The acid was distilled and reacted with KHCO₃. KFSI was recrystallized in ethanol. For IL synthesis, emim⁺(C₂H₅OSO₃)⁻ was obtained from the reaction of stoichiometric ethyl sulfate (Fluka) on distilled 1-methyl-imidazole (Aldrich) in CH₂Cl₂ at 0 °C. This hydrophilic IL was reacted in water with a 10% excess of either LiTFSI or KFSI, compensating a possible water uptake for air handling of hygroscopic LiTFSI. The denser phase separating immediately was diluted with CH₂Cl₂ and extracted in a separating funnel and washed four times with water, and the dichloromethane was stripped. The as prepared ILs were heated at 120 °C under a vacuum and transferred for handling in a helium-filled drybox (H₂O, O₂ < 1 ppm) and used to fill ≈1.5 cm deep o.d. 4 mm NMR tubes that were stoppered with a Torr seal in the drybox, and later flame-sealed with a H₂/O₂ torch outside. The same IL samples were measured by the Karl Fischer technique to be ≤30 ppm water content.

Pulsed-field gradient NMR (pfg-NMR) experiments were performed on these [emim][TFSI] and [emim][FSI] using a homemade spectrometer working at Larmor frequencies in the interval 30 MHz ≤ ν ≤ 300 MHz and a superconducting coil giving a direct magnetic field of 6.6 T. The magnetic field gradient pulses were delivered by a Techron power supply, the maximum constant current reaching 60 A during 5 ms. Details of the diffusion coefficient measurements have been given elsewhere.⁷⁹ Figure 2 shows the cation and anion self-diffusion coefficients for [emim][FSI] and [emim][TFSI] obtained from pfg-NMR measurements as a function of inverse temperature. Comparison of our self-diffusion coefficient measurements with previously reported data¹⁷ for [emim][TFSI] indicates that at high temperature our results are slightly lower, while at low temperatures our results are slightly higher. The temperature

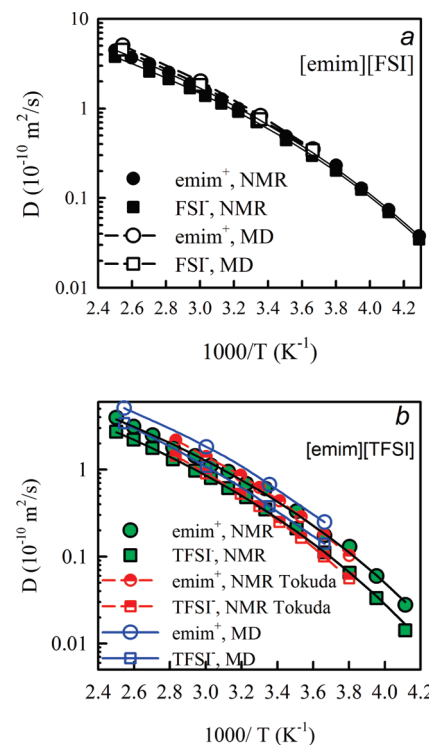


Figure 2. Self-diffusion coefficient of ions in [emim][FSI] (a) and [emim][TFSI] (b) from pfg-NMR experiments and MD simulations. Previous pfg-NMR data by Tokuda et al.¹⁷ are also shown in (b). Lines show the VTF fit to experimental data. (MD data have been corrected for the finite simulation cell size using eq 3.)

TABLE 1: Vogel–Fulcher–Tamman Parameters Fitted to Self-Diffusion Coefficients of IL from pfg-NMR Experiments^a

	D ₀ (10 ⁻¹⁰ m ² s ⁻¹)	B (K)	T ₀ (K)
[emim][FSI]			
emim ⁺	91.0	821	127.6
FSI ⁻	60.54	742.3	133.5
[emim][TFSI]			
emim ⁺	90.33	825.0	140.
TFSI ⁻	72.87	852.8	141.3
emim ⁺ , Tokuda et al.	130 ± 40	847 ± 119	146 ± 12
TFSI, Tokuda et al.	100 ± 10	903 ± 130	146 ± 13

^a Previously published parameters from Tokuda et al.¹⁷ are also given for comparison.

dependence of the self-diffusion coefficients was fit using Vogel–Fulcher (VF) relationship:

$$D = D_0 \exp\left(-\frac{B}{T - T_0}\right) \quad (1)$$

where *T* is temperature and *D*₀, *B*, and *T*₀ are fitted parameters given in Table 1. VF fits for [emim][TFSI] and [emim][FSI] indicate that *D*₀ and the high temperature activation energies *B* are quite similar. This similarity implies that cation motion is essentially independent of the particular anion at high temperature (*T* ≫ *T*₀). However, *T*₀ for emim⁺ is lower by about 10 K for [emim][FSI] than for [emim][TFSI], indicating the onset of glassy behavior at lower temperature for the former IL. This translates into increasingly faster motion of emim⁺ in [emim][FSI] relative to that in [emim][TFSI] with decreasing temperature, as illustrated in Figure 3. Similar behavior is observed

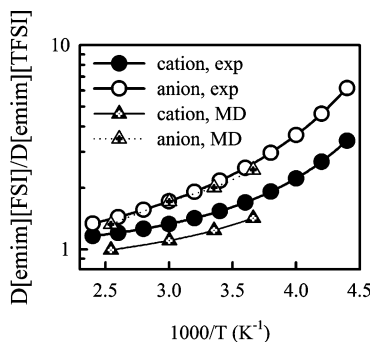


Figure 3. The ratio of the ion self-diffusion coefficients in [emim][FSI] to that in [emim][TFSI] from pfg-NMR experiments and MD simulations.

when FSI^- and TFSI^- self-diffusion coefficients are compared, as shown in Figure 3. However, in contrast to emim^+ , the high temperature activation energy for the anion does depend upon the particular anion, with that for TFSI^- being greater than that for FSI^- . Hence, even at temperatures well above the glass transition temperature, FSI^- and TFSI^- motions remain different.

III. Simulation Methodology

Simulations were performed using an improved version (f1e24) of the many-body polarizable force field,^{32,35} that demonstrated consistently accurate predictions of IL density, ion self-diffusion coefficients, conductivity, and viscosity.^{32–34} The crystal structure of four selected ionic crystals was also accurately predicted³² together with the conductivity of EC: DMC/LiPF₆ liquid electrolytes³⁶ and properties of semifluorinated alkanes,⁸⁰ alkyl nitrate liquids, and PETN energetic crystal.⁸¹ This force field (APPLE&P version f1e) has an improved transferability and allowed better prediction of ion transport compared to the previous force field generations developed by us^{82–85} that have been used in simulations of carbonate liquid electrolytes, polymer electrolytes, [pyr₁₃][TFSI], and [pyr₁₃][TFSI] doped with LiTFSI.^{82,83,85–88} Main force field features are briefly described here, while development methodology is outlined in detail elsewhere.³² Molecules were fully flexible with bending, and a conformational energetics were fit to quantum chemistry data, while bond lengths were constrained. Polarization was incorporated via an isotropic atomic dipole formalism using Thole screening ($a_T = 0.2$), while the electrostatic potential around molecules is described via permanent charges located on atoms and off-atom sites. For the TFSI and FSI^- anions, an extended charge (denoted as L_p, Figure 1a) in the S–N–S plane was included in the modified force field (f1e24) to provide an improved description of the electrostatic potential around anions as obtained from quantum chemistry calculations performed on the MP2/cc-pvTz level. Inclusion of this charge center in the force field has only a minor effect on the density and transport properties of ionic liquids reported here, but it is expected to be important for describing the FSI^- and TFSI^- interactions with the lithium cations. Interestingly, placing two additional force centers at the positions where lone pairs are expected on the nitrogen atom yielded a less significant improvement than was found for the single extended charge located within the S–N–S bend. In the f1e24 version of the force field the R^* (position of the minimum) of the repulsive-dispersive interactions was reduced by 6% for the F···F pair in the FSI^- anion, while R^* for the S···S pair was reduced by 3% from the corresponding parameters in the f1e1 force field to improve the density description of the ILs. The resulting

TABLE 2: Length of Simulation Production Runs and IL Properties from MD Simulations and Previously Published Experiments (in Parentheses)

ionic liquid	$N_{\text{ion pairs}}$	run length (ns)			
		393 K	333 K	298 K	273 K
[emim][TFSI]	150	15.3	14.4	16.8	18
[emim][FSI]	125	16.0	16.2	18	18
[pyr ₁₃][TFSI]	216	8.6	9.3	9.3	
[pyr ₁₃][FSI]	216	9.7	10.1	10.2	

ionic liquid	density (kg m ⁻³)			
	393 K	333 K	298 K	273 K
[emim][TFSI]	1435	1488	1521 (1522 ^a , (1487) ^a	1545 1517 ^b) (1547) ^a
[emim][FSI]	1347	1395	1426	1449
[pyr ₁₃][TFSI]	1358	1407	1434 (1408–1447) ^c	
[pyr ₁₃][FSI]	1266	1308	1339 (1339) ^d	

ionic liquid	viscosity (mPa s)		
	393 K	333 K	298 K
[emim][TFSI]	3.6	10.4	
[emim][FSI]	3.6	6.7	13.3
[pyr ₁₃][TFSI]	4.8	18.2	
[pyr ₁₃][FSI]	6.3	18.5	63.0

^a Reference 17. ^b Reference 75. ^c References 26 and 28. ^d Reference 23.

densities from MD simulations are compared with experimental data in Table 2, demonstrating excellent agreement between the two.

A version of the MD simulation package *Lucretius* that includes many-body polarization was used for all MD simulations.⁸⁹ A three-dimensional, periodic cubic simulation cell consisted of 125–216 ion pairs as shown in Table 2. The IL initial configurations were created in the gas phase corresponding to a cell (linear) dimension of approximately 75–90 Å. The dimensions of the simulation cells were reduced to yield estimated densities at 393 K followed by 0.8–2 ns NPT run. The average box sizes from the NPT runs were utilized in the subsequent NVT production runs. The length of production runs was always long enough to achieve the diffusive regime in ILs and is given in Table 2. Additional simulations 4–5 ns long were performed with the barriers for the anion conformational transitions increased by 12.5 kJ/mol at 298 K.

The Ewald summation method was used for electrostatic interactions between partial charges with partial charges and partial charges with induced dipole moments using k^3 from 6³ to 8³ k -vectors, and α from 8.5 to 12 Å depending on the system size. The interaction between an induced dipole and a partial charge separated by 3 bonds was scaled by 0.8, providing an improved description of the electrostatic potential around the molecules. Multiple time step integration with an inner time step of 0.5 fs (bonded interactions), a central time step of 1.5 fs for all nonbonded interactions within a truncation of 7.0 Å and an outer time step of 3.0 fs for all nonbonded between 7.0 Å and the nonbonded truncation distance of 10.5 or 11 Å as well as for the reciprocal part of Ewald was employed. A Nose–Hoover thermostat (NPT and NVT simulations) and a barostat (NPT simulations) were used to control the temperature and pressure with the associated frequencies of 10^{−2} and 0.5 × 10^{−3} fs. Induced dipoles were calculated via a direct iteration with a predictor method. Pressure tensor and virial were calculated using atom-based with bond (constrained) forces every 3 fs and saved every 9 fs for viscosity calculation.

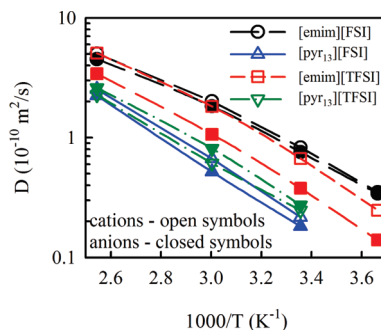


Figure 4. Ion self-diffusion coefficients of ILs obtained from MD simulations (corrected for the finite simulation cell size).

IV. Simulation Results

A. Ion Self-Diffusion Coefficients. The self-diffusion coefficient D_i for species i was calculated using the Einstein relation, by fitting the slope on the mean-square displacement $MSD(t)$ in the linear diffusive regime and dividing by six. The $MSD(t)$ and $a + bt^\beta$ local fits to the $MSD(t)$ for $[emim][FSI]$ and $[pyr_{13}][FSI]$ are shown in Supporting Information. These $MSD(t)$ and the local $a + bt^\beta$ fits to the $MSD(t)$ segments (a , b , and β are fit parameters) indicate that at 298 K the subdiffusive regime ($\beta < 1$) extends up to ~ 0.8 ns for $[pyr_{13}][FSI]$ and 0.3 ns for $[emim][FSI]$.

Due to the finite size of the simulation cell, long-range hydrodynamic interactions restrict diffusion.⁹⁰ The leading order finite size correction (FSC) to the self-diffusion coefficient (ΔD^{FSC}) was found to be inversely proportional to the simulation box and is given by⁹⁰

$$\Delta D^{FSC} = \frac{2.837k_B T}{6\pi\eta L} \quad (2)$$

where L is a linear dimension of the cubic simulation periodic cell, T is temperature, and η is viscosity. We utilized viscosity from MD simulations shown in Table 2 for calculating ΔD^{FSC} when possible. Viscosity was extracted using the Einstein relation, as described in our previous work.³² At low temperatures where the viscosity value from MD simulations was not available due to insufficient run length, the FSC correction from the high temperature was used. The finite size correction was 10–21% for the simulated ILs depending on the system size.

Figure 2 shows the finite size corrected self-diffusion coefficients from MD simulations are in excellent agreement with pfg-NMR data for $[emim][FSI]$ and $[emim][TFSI]$. MD simulations also correctly predict that the cation is diffusing slightly faster than the anion for $[emim][FSI]$ and noticeably faster for $[emim][TFSI]$ IL. Figure 3 shows that MD simulations adequately describe the enhancement of the ion diffusion coefficients in $[emim][FSI]$ relative to the cation and anion diffusion coefficients in $[emim][TFSI]$. Consistent with experiments, we observed that the anion diffusion coefficient is largely responsible for the faster ion transport in $[emim][FSI]$ compared to that in $[emim][TFSI]$.

Figure 4 compares ion self-diffusion coefficients for all four simulated ILs. Ion self-diffusion coefficients roughly follow the order $[emim][FSI] > [emim][TFSI] > [pyr_{13}][FSI] > [pyr_{13}][TFSI]$. In contrast to a significantly faster anion dynamics in $[emim][FSI]$ than in $[emim][TFSI]$, the difference between the ion diffusion coefficients in $[pyr_{13}][TFSI]$ and $[pyr_{13}][FSI]$ is less pronounced. Replacing the $TFSI^-$ with FSI^- results in a significant enhancement of the anion diffusion, while the cation

self-diffusion coefficients are similar for the corresponding FSI^- and $TFSI^-$ based ILs.

D. Conductivity and Correlated Ion Motion. Ionic conductivity can be calculated from MD simulations using the Einstein relation⁹¹

$$\lambda = \lim_{t \rightarrow \infty} \lambda(t) = \lim_{t \rightarrow \infty} \frac{e^2}{6tVk_B T} \sum_{i,j}^N z_i z_j \langle [\mathbf{R}_i(t) - \mathbf{R}_i(0)]([\mathbf{R}_j(t) - \mathbf{R}_j(0)]) \rangle \quad (3)$$

where e is the electron charge, V is the volume of the simulation box, z_i and z_j are the charges over ions i and j in electrons, $\mathbf{R}_i(t)$ is the displacement of the ion i during time t , the summation is performed over all ions N in the simulation cell, $\langle \rangle$ denote the ensemble average. Here $\lambda(t)$ is the apparent time-dependent conductivity whose long-time limit corresponds to the equilibrium dc conductivity of an electrolyte. Conductivity can be decomposed into an “ideal” conductivity that would be realized if ion motion were uncorrelated, denoted λ_{uncor} , and the degree to which ion motion is in fact uncorrelated, or α_d . The apparent degree of uncorrelated ion motion $\alpha_d(t)$ is given as the ratio of the apparent collective (total) charge transport $\lambda(t)$ to the apparent charge transport due to self-diffusion only $\lambda_{uncor}(t)$, hence

$$\lambda_{uncor} = \lim_{t \rightarrow \infty} \lambda_{uncor}(t) = \lim_{t \rightarrow \infty} \frac{e^2}{6tVk_B T} \sum_i^N z_i^2 \langle [\mathbf{R}_i(t) - \mathbf{R}_i(0)]^2 \rangle = \frac{e^2}{V k_B T} (n_+ D_+^{app} + n_- D_-^{app}) \quad (4)$$

$$\alpha_d = \frac{\lambda}{\lambda_{uncor}} = \lim_{t \rightarrow \infty} \alpha_d(t) = \lim_{t \rightarrow \infty} \frac{\lambda(t)}{\lambda_{uncor}(t)} \quad (5)$$

Here n_i is the number of ions of type i . A degree of ion uncorrelated motion $\alpha_d(t) = 1$ corresponds to completely uncorrelated ion motion, while $\alpha_d(t) = 0$ if all of the cations only move together with anions (which corresponds to $\lambda = 0$, i.e., zero ionic conductivity). Determining the long-time limit of $\lambda(t)$ using eq 3 is problematic because of poor statistics in the diffusive regime. Instead, we determine the IL conductivity as a product of λ_{uncor} derived from self-diffusion coefficients using eq 4 and α_d extracted from the sub diffusive regime but with good statistics. An example of $\alpha_d(t)$ for $[emim][FSI]$ IL is shown in Supporting Information, Figure S3. We observe an initial increase of the α_d value followed by the plateau indicating decrease of ion correlation with time as ions escape the cages. Our experience indicates that $\alpha_d(t)$ results are accurate only up to the times approximately 2–5% of the total simulation run, consistent with similar claims for extracting viscosity from MD simulations;⁹² therefore we extracted α_d value from the plateau of $\alpha_d(t)$ in the region of 100–200 ps. The α_d values for simulated ILs are in the region of 0.55–0.75. Similar values of $\alpha_d(0.52–0.78)$ have been reported from the coordinated pfg-NMR and conductivity measurements^{16,17,93} of $[emim][TFSI]$, $[bmim][PF_6]$, $[bmim][BF_4]$, $[bmim][TFSI]$, $[bmim][CF_3SO_3]$, $[C_6mim][TFSI]$, $[pyr_{14}][TFSI]$, $[N_{1114}][TFSI]$, and simulations.⁷⁰ Nicotera et al.²⁸ also reported unusually low value α_d of 0.28 for $[pyr_{13}][TFSI]$ at 333 K, while MD simulations predict α_d of 0.63 at 333 K, which is in line with the $\alpha_d = 0.7$ experimentally found by Tokuda et al.⁹³ for $[pyr_{14}][TFSI]$.

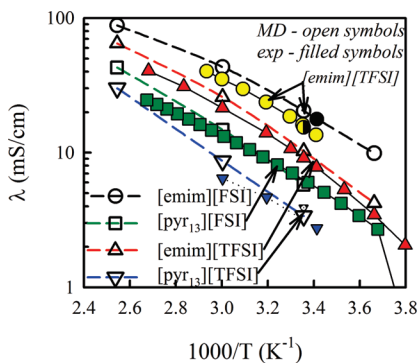


Figure 5. Conductivity of ILs obtained from MD simulations and the following experiments: [pyr₁₃][FSI] from Zhou et al.,²² [pyr₁₃][TFSI] from Nicotera et al.;²⁸ [emim][FSI] from Guerfi et al.²⁴ (black filled circle), Kikuta et al.⁹⁴ (yellow filled circle), and Matsumoto et al.¹⁹ (semifilled circle); [emim][TFSI] from Tokuda et al.¹⁷

The resulting ionic conductivities from MD simulations are compared with experiments^{17,19,22,24,28,94} in Figure 5. At room temperature an excellent agreement between experimental and simulation conductivity has been observed for all simulated ILs. The predicted [emim][FSI] conductivity agrees perfectly with the experimental data by Guerfi et al.,²⁴ which is slightly higher than the values reported by Kikuta et al.⁹⁴ and Matsumoto et al.¹⁹ MD simulations also predicted the temperature dependence of [emim][TFSI], [pyr₁₃][FSI], and [emim][FSI] in good agreement with experiments.^{17,22,94} The temperature dependence of [pyr₁₃][TFSI] from experiments differs from that observed in MD simulations; however, we previously reported an excellent prediction of the temperature dependence of ion conductivity and self-diffusion coefficients for the closely related [pyr₁₄][TFSI], giving us additional confidence in the accuracy of our predictions for [pyr₁₃][TFSI]. It is probably that the unusually low α_d of 0.28 for [pyr₁₃][TFSI] reported by Nicoreta et al.²⁸ stems from the low experimental conductivity of [pyr₁₃][TFSI] at 333 K shown in Figure 5. Further examination of Figure 5 indicates that conductivity of ILs are ordered as follows at room temperature: [emim][FSI] > [emim][TFSI] > [pyr₁₃][FSI] > [pyr₁₃][TFSI]. While the ordering of conductivities is similar to the ordering of the ion self-diffusion coefficients shown in Figure 4, the enhancement of conductivity upon replacing TFSI⁻ and FSI⁻ is more pronounced than the effect observed for the ion self-diffusion coefficients because the smaller size of the FSI⁻ anion compared to that for TFSI⁻ results in a higher ion number density leading to an additional enhancement of the conductivity for the FSI-based ILs. Lower activation energy is seen for [emim][FSI] than for [emim][TFSI], and [pyr₁₃][FSI] than for [pyr₁₃][TFSI], which is consistent with the analysis of the temperature dependence of ion self-diffusion coefficients presented in Figures 3 and 4.

C. Conformational Populations and Dynamics. The TFSI⁻ and FSI⁻ anions have two low energy conformations gg and g⁺g⁻,⁷⁵ where conformations are given around the F-S-N-S and C_{F3}-S-N-S dihedral angles. These conformers are also referred to as trans and cis conformations around F-S...S-F and C-S...S-C dihedrals for FSI⁻ and TFSI⁻ anions, respectively. The trans conformer is more stable than the cis conformer by about 1 kcal/mol (4.184 kJ/mol) for both TFSI⁻ and FSI⁻ anions according to quantum chemistry calculations^{32,50,95} and analysis of Raman spectra.^{76,95} The distribution of TFSI⁻ and FSI⁻ conformational populations in ILs from MD simulations is shown in Figure 6. The FSI⁻ and TFSI⁻ anion conformational populations indicate a significant difference between each other, which is consistent with previous reports.^{38,50} Figure 6 also

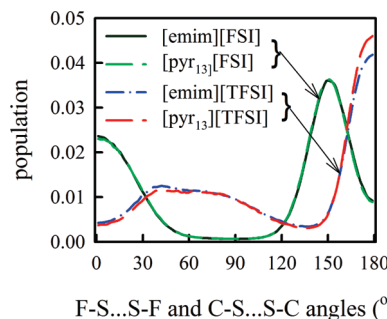


Figure 6. Distribution of conformational populations for FSI⁻ and TFSI⁻ anions around F-S...S-F and C-S...S-C dihedrals for ILs at 298 K.

TABLE 3: Apparent Activation Energy (in kJ/mol) for IL Transport Properties: Diffusion (E_{diff}), Conformational Relaxation Measured via Torsional ACF (E_{tor}), and the Trans Conformer Populations for Anions (E_{trans})

	E_{diff}	E_{tor}	E_{trans}	
	D_+	D_-	τ_{tor}	anion
[emim][FSI]	17.8	17.6	16.8	2.1
[emim][TFSI]	19.8	21.7	21.4	2.1
[pyr ₁₃][FSI]	23.5	21.8	17.8	2.4
[pyr ₁₃][TFSI]	24.8	26.7	22.8	3.3

indicates that the TFSI⁻ and FSI⁻ conformational populations are the same for the emim⁺-containing IL and pyr₁₃⁺-containing ILs. Moreover, the anion conformational populations were found to be similar in the gas phase and liquid phases. However, we observed a significantly higher peak for the FSI⁻ trans conformer at 150° than for the cis conformer at 0°, while Canongia Lopes et al.⁵⁰ have reported a similar magnitude for those peaks. Similarly, the peak for the TFSI⁻ trans conformer is about a factor of 3 larger than the peak for the cis conformer located around 40°, while in Canongia Lopes et al.³⁷ simulations the difference was less than 1.5 for [pyr₁₄][FSI] at 298 K. The trans populations were calculated by integrating distributions from 90° to 180° for FSI-based ILs and from 130° to 180° for the TFSI-based ILs. We obtained for following populations of trans conformers at 298 K: 0.643 for [emim][FSI], 0.632 for [pyr₁₃][FSI], 0.565 for [emim][TFSI], and 0.468 for [pyr₁₃][TFSI]. These conformational populations are in agreement with the analysis of Raman measurements for [pyr₁₃][TFSI],⁹⁶ [pyr₁₃][FSI],²³ and [emim][TFSI]²³ that indicated that a similar fraction of cis and trans conformers were found in these ILs near room temperature. In agreement with analysis of Raman experiments,^{23,96} MD simulations predict that the fraction of trans conformers increases with decreasing temperature. The activation energies were calculated for the trans conformational populations by fitting populations vs inverse temperature to the Arrhenius behavior and are given in Table 3. These activation energies are in agreement with the fits to Raman measurements for [pyr₁₃][TFSI],⁹⁶ [pyr₁₃][FSI],²³ and [emim][TFSI].²³

We have monitored the dynamics of anion conformational transitions via torsional autocorrelation function (ACF) given by eq 6.

$$P_{\text{ACF}}(t) = \frac{\langle \cos(\phi(t)) \cos(\phi(0)) \rangle - \langle \cos(\phi(0)) \rangle^2}{\langle \cos^2(\phi(t)) \rangle - \langle \cos(\phi(0)) \rangle^2} \quad (6)$$

where $\phi(t)$ is the O-S-N-S dihedral angle, t is time, and the brackets denote an ensemble and time average over all dihedrals.

The torsional ACFs were fit with Kohlrausch–Williams–Watts (KWW) stretched exponential functions for $P_{\text{ACF}}(t) > 0.01$ given by eq 7

$$P_{\text{KWW}}(t) = A \exp\left[-\left(\frac{t}{\tau_{\text{KWW}}}\right)^{\beta}\right] \quad (7)$$

where β determines the degree of stretching characterizing the broadness of the relaxation process, and the A prefactor allows us to account for decay that occurs in a time span significantly faster than our minimum data collection rate of 1 ps^{-1} . A is typically $0.95–1.0$. The stretched exponential fits yielded the degree of the relaxation process broadness β of 0.9 for the FSI^- anion in $[\text{emim}][\text{FSI}]$ and $[\text{pyr}_{13}][\text{FSI}]$, while β for the TFSI^- anion was around 0.6 for $[\text{emim}][\text{TFSI}]$ and $[\text{pyr}_{13}][\text{TFSI}]$, indicating a much broader relaxation spectrum for the latter. The torsional relaxation times were calculated as integrals of $P_{\text{KWW}}(t)$ fits from zero to infinity. The apparent activation energies for the torsional relaxation times (E_{tor}) were calculated and are compared in Table 3 with the apparent activation energy for the average self-diffusion coefficients. The activation energy and absolute values for torsional relaxation time for the FSI^- anion in $[\text{emim}][\text{FSI}]$ and $[\text{pyr}_{13}][\text{FSI}]$ are essentially identical despite a significant difference observed between the ion self-diffusion coefficients in these two ILs. While the activation energy for torsional relaxation of FSI^- is only slightly less than the activation energy for the anion self-diffusion coefficient for $[\text{emim}][\text{FSI}]$, a significantly smaller activation energy for the torsional relaxation E_{tor} compared to the activation energy for diffusion was observed for $[\text{pyr}_{13}][\text{FSI}]$, suggesting a decoupling between the FSI^- conformational relaxation and diffusion. A large β -broadness parameter of $0.91–0.94$ for the stretched exponent fit is also consistent with decoupling of torsional relaxation from the matrix relaxation. For example, a high β -broadness parameter and low activation energy for the torsional relaxation time was found for isolated polyethylene chains compared to the case for the polyethylene melt.⁹⁷ Unlike the FSI^- anion conformational relaxation, the TFSI^- anion conformational relaxation is characterized by a β -broadness parameter of $0.6–0.65$, indicative of the TFSI^- conformational relaxation coupled to the matrix relaxation.

To confirm our supposition about decoupling of the FSI^- anion conformation relaxation from ion diffusion and understand the extent to which TFSI^- conformational dynamics is coupled to ion diffusion, we have performed MD simulations of $[\text{emim}][\text{FSI}]$, $[\text{pyr}_{13}][\text{FSI}]$, $[\text{emim}][\text{FSI}]$, and $[\text{pyr}_{13}][\text{TFSI}]$ ILs with the FSI^- and TFSI^- conformation relaxation slowed down by approximately a factor of $100–200$. This was achieved by increasing the barriers for conformational transitions by 12.5 kJ/mol , without influencing the relative conformational energies of the trans and cis conformers of anions. In $[\text{emim}][\text{FSI}]$ with the increased FSI^- barriers the estimated $\text{O}–\text{S}–\text{N}–\text{S}$ dihedral relaxation time increased from 0.145 ns to $\sim 18 \text{ ns}$, allowing FSI^- to diffuse 680 \AA^2 during this time, indicating that anions diffuse long distances without undergoing conformational relaxation and, therefore, could be considered as rigid anions. We found that the cation and anion self-diffusion coefficients of $[\text{emim}][\text{FSI}]$ and $[\text{pyr}_{13}][\text{TFSI}]$ remained unchanged when the FSI^- anion conformational relaxation was significantly retarded, thus confirming that the FSI^- conformational relaxation is indeed decoupled from the ion translational motion. Slowing down the TFSI^- conformational relaxation, on the other hand, resulted in a slowing down of the ion diffusion in $[\text{emim}][\text{TFSI}]$ and $[\text{pyr}_{13}][\text{TFSI}]$ by $40–50\%$, thus confirming coupling, albeit

weak, between the TFSI^- conformational relaxation, ion diffusion and matrix relaxation.

E. Rotational Relaxation. We investigated the rotational motion of ion by examining the motion of the three vectors shown in Figure 1. $P_1(t)$ rotational ACF of the vectors are given by

$$P_1(t) = \langle \vec{e}(t) \cdot \vec{e}(0) \rangle \quad (8)$$

where $\vec{e}(t)$ is a unit vector corresponding to one of the three vectors shown in Figure 1. Decay of the $P_1(t)$ autocorrelation functions to 0.01 obtained from MD simulations was approximated by a stretched exponential expression given by eq 7.

Rotational autocorrelation times τ_1 were calculated as the time integrals of the KWW fits to $P_1(t)$ from zero to infinity. The τ_1 autocorrelation times are shown in Figure 7 as a function of inverse temperature. Rotation of the emim^+ x -axis, pyr_{13}^+ y -axis, and FSI^- and TFSI^- x -axis are the slowest as the molecules are the longest in these directions, as roughly indicated by components of the mean-square radii of gyration for emim^+ ($3.24, 0.80, 0.274 \text{ \AA}$), pyr_{13}^+ ($0.87, 3.06, 1.17 \text{ \AA}$), FSI^- ($2.59, 0.51, 0.61 \text{ \AA}$), and TFSI^- ($3.83, 0.85, 1.76 \text{ \AA}$) ions. Replacement of the TFSI^- anion with FSI^- only slightly increases rotation relaxation of cations, while rotational relaxation of the FSI^- anion is much faster than that of the TFSI^- anion in accord with the trends observed for the self-diffusion coefficients. The apparent activation energies for the rotational relaxation time were calculated from Arrhenius fits to τ_1 autocorrelation times and were found to be similar (within 3 kJ/mol) to the apparent activation energies for the ion self-diffusion coefficients shown in Table 3.

Further comparison between temperature dependence of the rotational and translational relaxations was achieved by investigation of the product of the ion self-diffusion coefficient and rotational relaxation time (τ_{RD}) shown in Figure 8 as a function of temperature. All plots were scaled to bring them to 1.0 at 393 K . If the product of τ_{RD} does not change with temperature, it indicates that the translational and rotational relaxation have the same temperature dependence. A decrease of the (τ_{RD}) product with decreasing temperature indicates that the ion self-diffusion coefficient decreases faster than the rotational relaxation time increases with temperature decrease. We observe that for all ILs the (τ_{RD}) product slightly decreases with decreasing temperature, thus indicating that the ion rotational relaxation has a slightly weaker temperature dependence than the translational relaxation, but the effect is not large. The smallest deviation of the product from unity was observed for the emim^+ cation in $[\text{emim}][\text{FSI}]$ followed by the emim^+ cation in $[\text{emim}][\text{TFSI}]$, while the largest deviation from unity was observed for the y -axis (see Figure 1) of TFSI^- . Thus, the fastest rotation of the TFSI^- anion shows the largest decoupling from the translational ion relaxation.

F. Structural Properties. Structure factor was calculated using eq 9 for ILs,

$$S(k) = 1 + \frac{\sum_{\alpha\beta} x_\alpha x_\beta f_\alpha(k) f_\beta(k) 4\pi \int_0^{r_c} (g_{\alpha\beta}(r) - 1) r^2 \frac{\sin(rk)}{rk} dr}{(\sum_\alpha x_\alpha f_\alpha(k))^2} \quad (9)$$

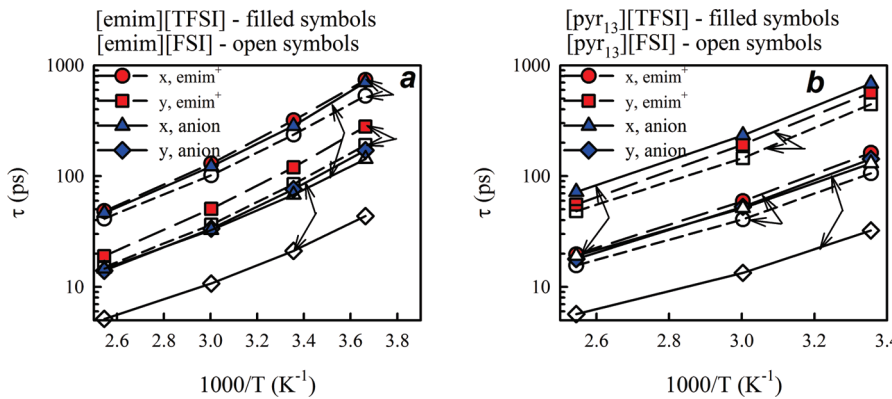


Figure 7. Rotational relaxation times of IL from MD simulations. Arrows point to the same cation and anion rotational modes in the FSI-based ILs (open symbols) and TFSI-based ILs (filled symbols).

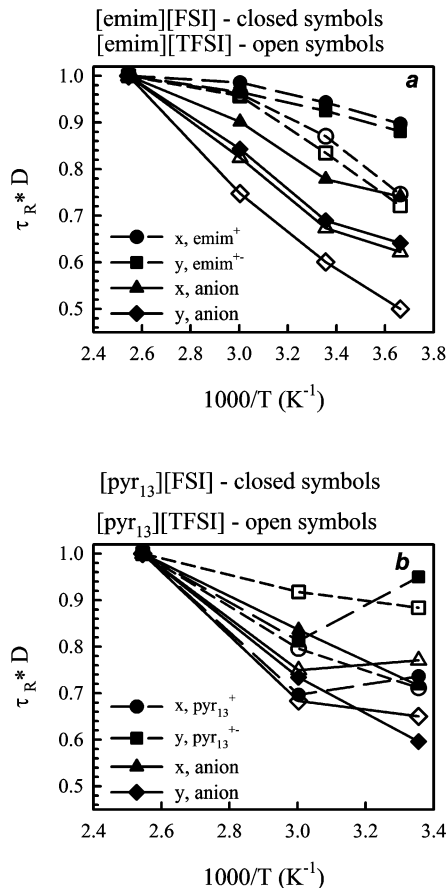


Figure 8. Product of the rotational relaxation time and the ion self-diffusion coefficients.

where x_α and x_β are the fractions of atoms of type α and β , $g_{\alpha\beta}(r)$ is the radial distribution function (RDF) for α and β atom types, k is the wave vector, $f_a(k)$ is the form factor for species a , and r_c is the cutoff for integration equal to half of the simulations box. Parts a and b of Figure 9 show the structure factor for ILs calculated from MD simulations and X-ray diffraction measurements. An excellent agreement between simulation predictions and X-ray measurements has been observed for [emim][TFSI], [pyr₁₃][FSI], and [pyr₁₄][TFSI], further demonstrating the ability of the developed force fields to accurately capture the ionic liquid structure, including the presence of two peaks in the low k value region (0.8 – 1.4 \AA^{-1}). A more detailed examination of Figure 9b indicates that replacement of TFSI⁻ with FSI⁻ results in a significant increase in the second peak for both emim⁺- and pyr₁₃⁺-based ILs, while

the magnitude of the second peak also increases upon replacing emim⁺ with pyr₁₃⁺. To understand which ion correlations contribute to the first and second peaks, the cation–cation, anion–anion, and cation–cation contributions to the IL structure factor were calculated and are shown in Figure 10. The cation–cation and anion–anion correlations contribute to the first $S(k)$ peak, while the cation–anion correlations make a large negative contribution to the first peak. The cation–anion correlations make the most significant contribution to the second $S(k)$ peak shown in Figure 10, while for [emim][FSI] and [pyr₁₃][FSI] the FSI–FSI correlations also contribute to the second peak around 1.2 \AA^{-1} .

The neutron weighted structure factors were calculated for ILs by assuming complete deuteration of cations and are compared with the X-ray weighted $S(k)$ in Figure 11. A significant difference between the X-ray and neutron $S(k)$ were observed, particularly for the FSI⁻ anion-containing ILs. For pyr₁₃⁺-containing ILs the magnitude of the first peak is larger for the neutron $S(k)$ than for the X-ray $S(k)$, while the opposite behavior was observed for the second peak. We associate this difference between the neutron and X-ray $S(k)$ with the significantly larger contribution of sulfur to the X-ray $S(k)$ than to the neutron weighted $S(k)$. In fact, making sulfur form factor $f(k)$ zero reduces the [pyr₁₃][FSI] second X-ray weighted $S(k)$ peak by a factor of 3. On the other hand, setting the neutron scattering length of sulfur to zero essentially does not change the second peak while slightly increasing the first peak. Examination of the [emim][TFSI] and [emim][FSI] $S(k)$ indicates that the magnitudes of the first peak for the neutron $S(k)$ is smaller than the magnitudes for the X-ray $S(k)$.

We continue comparison of structure in the four ILs by analyzing the center of mass radial distribution functions (RDFs) shown in Figure 12. We found very little difference for RDFs calculated from simulations with 216 and 100 ion pairs for [pyr₁₃][TFSI], indicating that artifacts due to the finite simulation box are not expected to occur for the investigated box sizes. The cation–cation center of mass RDF shows a higher first peak for the FSI-based ILs compared to that for TFSI-based ILs, while the magnitude of the first anion–cation peak is similar to those for the FSI-based and TFSI-based ILs. The magnitude of the first anion–cation peak is larger for the pyr₁₃⁺-based ILs than for the emim⁺-based ILs, suggesting a stronger structuring of the anion–cation in the pyr₁₃⁺-based ILs than in the emim⁺-based ILs. The TFSI–TFSI-RDF first peak is consistently higher than the FSI–FSI⁻ one, while the FSI⁻ anions exhibit closer approaches to each other than the TFSI⁻ anions due to the smaller size of the FSI⁻ anion. The smaller size of the FSI⁻

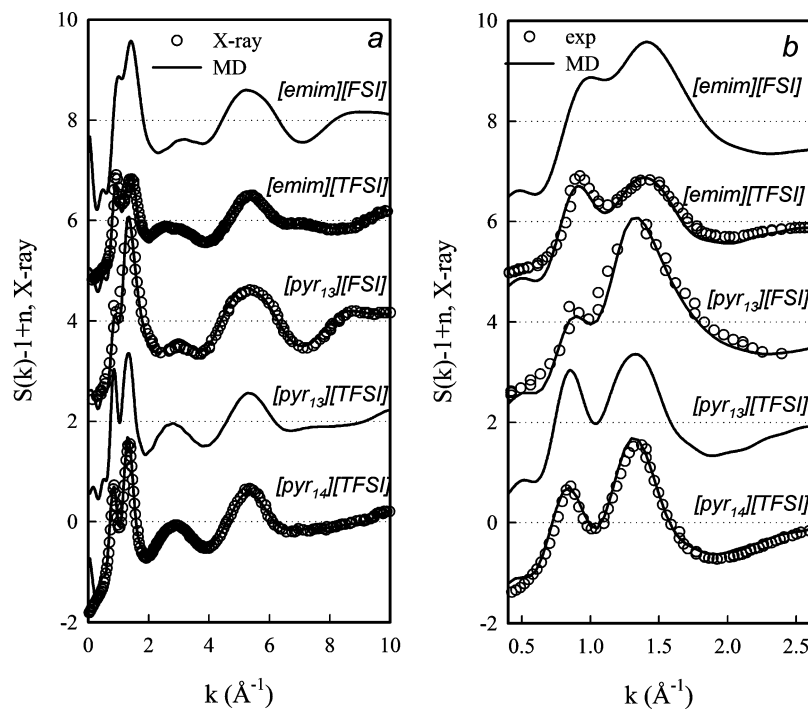


Figure 9. X-ray weighted structure factor $S(k)$ at 298 K from MD simulations and experiments.^{23,63,75}

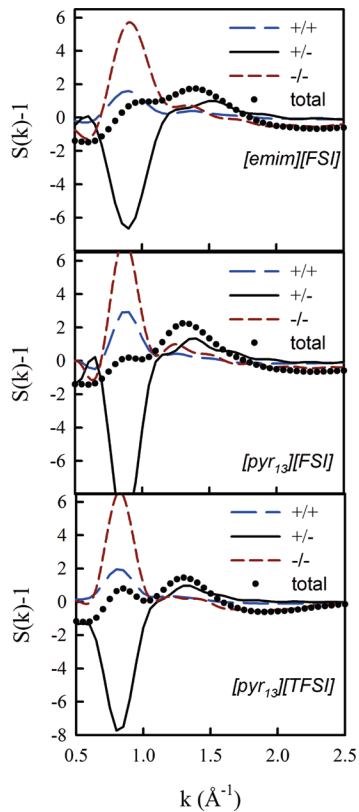


Figure 10. Cation–cation, anion–anion, and cation–anion contributions to the X-ray weighted structure factor $S(k)$ at 298 K from MD simulations.

anion is consistent with the shift of the $S(k)$ first and second peak positions to higher wave vectors, as shown in Figure 9.

The RDFs for the oxygen atom of FSI^- and TFSI^- with the emim^+ ring hydrogen are shown in Figure 13. The positions of the first peak are similar for $[\text{emim}][\text{TFSI}]$ and $[\text{emim}][\text{FSI}]$, whereas the magnitude of the first peak is larger for the $[\text{emim}][\text{TFSI}]$ than for the $[\text{emim}][\text{FSI}]$. Despite the larger

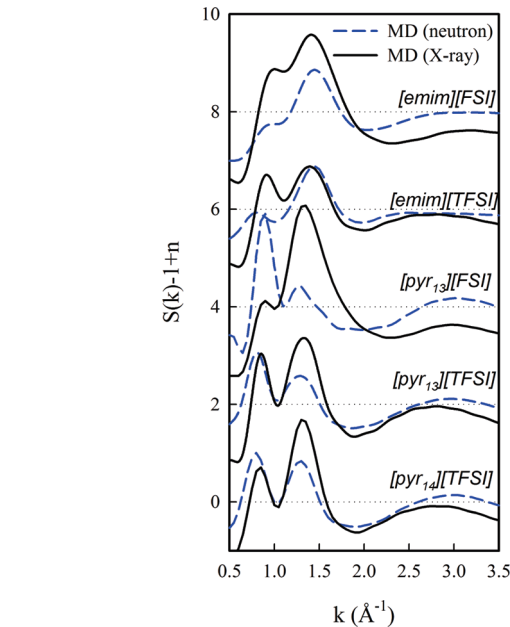


Figure 11. Neutron (deuterated) and X-ray weighted structure factors $S(k)$ for ILs at 298 K calculated from MD simulations.

magnitude of the first peak for the O–H RDF for $[\text{emim}][\text{TFSI}]$ compared to that for $[\text{emim}][\text{FSI}]$ the coordination number of oxygen atoms from FSI^- and TFSI^- anions near emim^+ ring hydrogen atoms is essentially the same: at 3.3 Å cutoff, 1.2 anion oxygen atoms are coordinating H(C_4) and H(C_5) hydrogens, and 1.7 anion oxygen atoms are coordinating H(C_2) hydrogen.

The 3D distributions of anion oxygen atoms are shown in Figure 14. The isosurfaces for the TFSI^- oxygen atoms have been scaled by the ratio of the number densities of $[\text{emim}][\text{FSI}]$ / $[\text{emim}][\text{TFSI}]$ and $[\text{pyr}_{13}][\text{FSI}]$ / $[\text{pyr}_{13}][\text{TFSI}]$ to reflect the coordination number of the oxygen atoms. Figure 14 clearly shows that the FSI^- and TFSI^- anion oxygen atoms pack (coordinate) in a very similar way around emim^+ and pyr_{13}^+

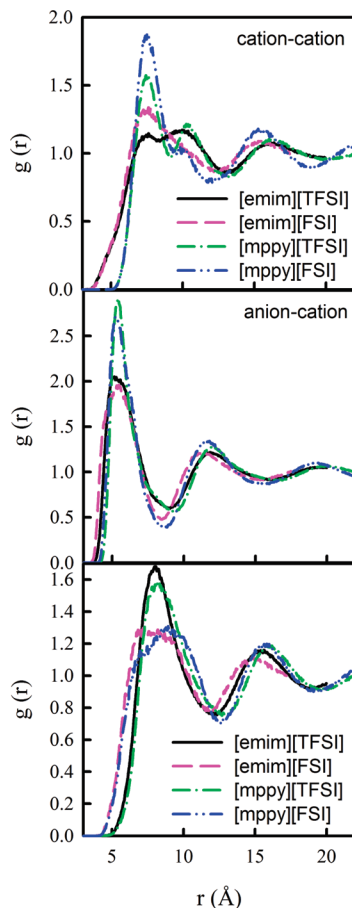


Figure 12. Center of mass radial distribution functions from MD simulations at 298 K.

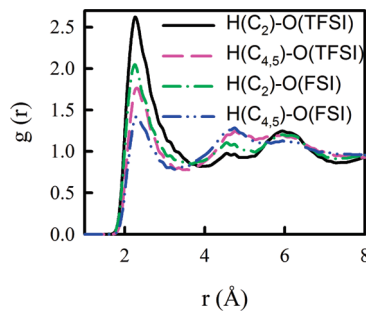


Figure 13. Radial distribution functions for [emim][FSI] and [emim]-[TFSI] from MD simulations at 298 K.

cations; specifically, not only the locations of the anion oxygen atoms around cations are the same but also the magnitudes of the scaled isosurfaces are indicative of the same coordination numbers.

Next we consider the relation between ion packing in the crystal phase to that in the liquid. While the most detailed information of the ion packing is typically obtained from X-ray diffraction measurements in the crystal phase, most IL liquids are utilized in the liquid phase that is more challenging to characterize experimentally at the same level of detail. MD simulations allow a detailed characterization of the structure in both the crystal and liquid phases. Here we utilize our simulations to understand differences in the crystal and liquid state ion packing. Figure 15 shows the position of anion oxygen atoms in the crystal phase from our previous simulations³² as a red wireframe and their positions in the liquid as green isosurfaces. While there is some overlap between the oxygen

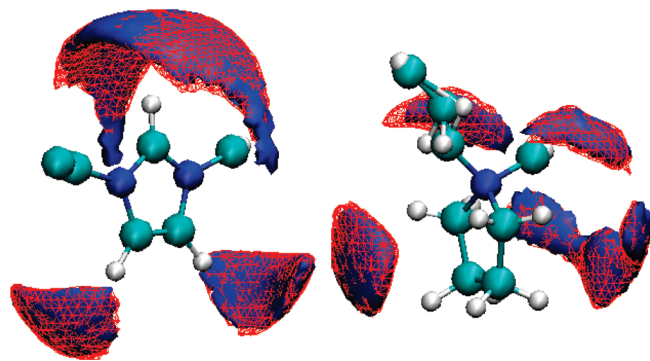


Figure 14. Isosurface of O atom of FSI^- (blue solid surface) and TFSI^- (red wireframe) anions around emim^+ and pyr_{13}^+ at 298 K for $\rho/\rho_{\text{random}} = 5$ (volume distribution function yielding 5 times the bulk average oxygen atom density) for [emim][FSI] and [pyr₁₃][FSI]. For the TFSI-based IL, $\rho/\rho_{\text{random}} = 6.2$ for [emim][TFSI] and $\rho/\rho_{\text{random}} = 6.07$ for [pyr₁₃][TFSI] were used to correct for the difference in bulk oxygen density in the FSI^- and TFSI-based ILs.

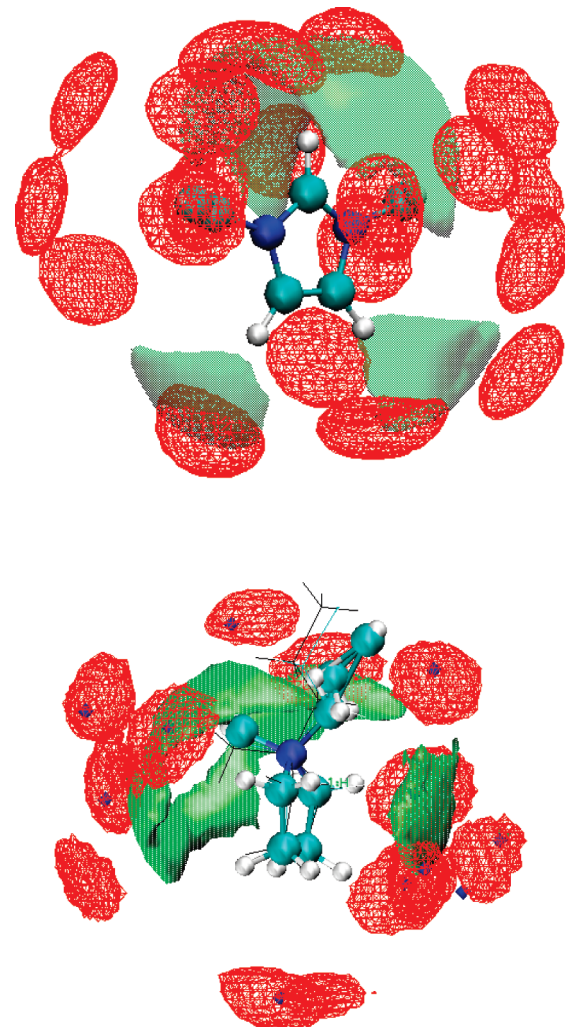


Figure 15. Positions of the TFSI^- anion oxygen atoms around emim^+ and pyr_{13}^+ cations from MD simulations of [emim][TFSI] and [pyr₁₃][TFSI] in the liquid (green isosurface $\rho/\rho_{\text{random}} = 5$) and the crystal (red isosurface $\rho/\rho_{\text{random}} = 5$). The most probable positions of TFSI^- anion oxygen atoms from X-ray experiments for [pyr₁₃][TFSI] are shown in blue.⁹⁸

positions in the crystal phase and in the liquid, little resemblance is found between the anion packing in the crystal and liquid phases; thus, X-ray crystal data should be used with caution for gleaned the insight into ion packing in the liquid phase.

TABLE 4: Ionic Liquid Structural and Thermodynamic Properties (Definitions in Text)

	$G_0^{\max}(r)$	H_{vap} (kJ/mol)	E_{\pm} (kJ/mol)	V_m (nm $^{-3}$)
[emim][TFSI]	15.3	123.9	342.9	0.427
[emim][FSI]	11.7	134.6	330.7	0.339
[pyr ₁₃][TFSI]	35.2	137.3	334.2	0.473
[pyr ₁₃][FSI]	25.5	143.9	326.5	0.382

G. Relation between Ion Transport with Thermodynamic Properties and Ionic Liquid Structure. Self-diffusion coefficients are different by a factor of 5 between four ILs considered. What accounts for such a difference of the self-diffusion coefficient for emim⁺-based vs pyr₁₃⁺-based IL or for TFSI⁻ and FSI⁻-based ILs? Four parameters that can potentially influence ion self-diffusion are (a) ion size, (b) cation–anion binding energy, (c) enthalpy of vaporization, and (d) packing of ions in IL. Analysis of the 3-D distributions shown in Figure 14 shows that the anion oxygen atoms are located in the four well-separated zones around pyr₁₃⁺, while only three disconnected locations of the anion oxygen atoms are observed around emim⁺. Moreover, a large connected zone (domain) of anion oxygens around the C₂ carbon of emim⁺ indicates that the anion can easily explore a large area without significant free energy barriers, while for an anion to relax (move) around pyr₁₃⁺ it should jump from one domain to another via the region with a low probability. A significantly larger first peak of the cation–anion RDF shown in Figure 13 for the pyr₁₃⁺-based ILs compared to that for the emim⁺-based ILs also indicates a stronger free energy for the cation–anion interaction in a liquid for the former. The maximum of the 3-D distribution function of the anion oxygen atom (denoted as G_0^{\max} in Table 4) is also significantly larger for pyr₁₃⁺-based ILs than for emim⁺-based ILs, further indicating stronger anion coordination around pyr₁₃⁺ than around emim⁺. A comparison of G_0^{\max} for [emim][TFSI] with [emim][FSI] and [pyr₁₃][TFSI] with [pyr₁₃][FSI] yields the ratios of $G_0^{\max}[\text{emim}][\text{FSI}]/G_0^{\max}[\text{emim}][\text{TFSI}] = 0.76$ and $G_0^{\max}[\text{pyr}_{13}][\text{FSI}]/G_0^{\max}[\text{pyr}_{13}][\text{TFSI}] = 0.72$. However, after correction for the difference of the oxygen atom number density in TFSI⁻ and FSI⁻ based ILs, these ratios become 0.95 and 0.87, indicating that the coordinations of cations by TFSI⁻ and FSI⁻ are similar, which is in accord with the above discussion and 3-D distributions shown in Figure 14. We conclude that the ion packing considerations cannot explain faster dynamics in [emim][FSI] compared to those in [emim][TFSI]. A smaller size of the FSI⁻ anion than for the TFSI⁻ anion (see Table 4), however, is most likely a reason behind the faster transport in [emim][FSI] than in [emim][TFSI], as the smaller size of the emim⁺ cation compared to that of the pyr₁₃⁺ cation is also consistent with the faster transport in emim⁺-based ILs compared to that in pyr₁₃⁺-based ILs.

In our recent work we investigated a number of correlations between the heat of vaporization H_{vap} , cation–anion binding energy (E_{\pm}), ion sizes expressed through molar volumes (V_m), and the self-diffusion coefficient (D) for 29 ionic liquids. A significant correlation between D and H_{vap} has been found, while the best correlation was found for $-\log(DV_m)$ vs $H_{\text{vap}} + 0.28E_{\pm}$, where the term $H_{\text{vap}} + 0.28E_{\pm}$ serves as a measure of the effective cohesive energy for ionic liquids. Table 4 suggests that diffusion trends for the FSI⁻ and TFSI⁻-based ILs cannot be correlated with H_{vap} ; however, we found that $H_{\text{vap}} + E_{\pm}$ correlates well with (DV_m) , as shown in Figure 15, suggesting that the faster diffusion in [emim][FSI] than in [emim][TFSI] could be attributed to the lower cation/anion binding energy and smaller size of FSI⁻ compared to those for TFSI⁻.

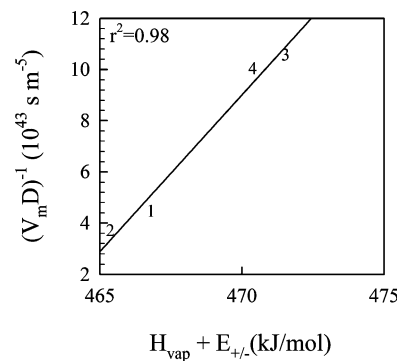


Figure 16. Correlation between the ion average self-diffusion coefficient (D) multiplied by the volume of the ion pair vs the enthalpy of vaporization (H_{vap}) plus the cation–anion binding energy (E_{\pm}) at 298 K: (1) [emim][TFSI]; (2) [emim][FSI]; (3) [pyr₁₃][TFSI]; (4) [pyr₁₃][FSI].

V. Conclusions

The pfg-NMR measurements have been performed over a wide temperature range on [emim][TFSI] and [emim][FSI] ILs focusing on the influence of anion on the ion dynamics. Replacing the TFSI⁻ anion in [emim][TFSI] IL with FSI⁻ resulted in a much faster diffusion of the anion in [emim][FSI] compared to that in [emim][TFSI], while the emim⁺ cation dynamics increased to a much smaller extent. Because of a lower apparent activation energy for the temperature dependence of the ion self-diffusion coefficients in [emim][FSI] compared to those in [emim][TFSI], the ratio of the ion diffusion coefficients in [emim][TFSI] to those in [emim][FSI] increases with decreasing temperature.

MD simulations were performed on [emim][TFSI], [emim][FSI], [pyr₁₃][TFSI], and [pyr₁₃][FSI] ILs. An excellent agreement was obtained between the ion self-diffusion coefficients of [emim][FSI] and [pyr₁₃][TFSI] extracted from MD simulations with the measured values from pfg-NMR experiments and available conductivity data. The X-ray structure factor for [emim][TFSI], [pyr₁₃][FSI], and [pyr₁₄][TFSI] from MD simulations agreed well with results of X-ray diffraction measurements. The pyr₁₃⁺ and emim⁺ cation coordination by TFSI⁻ anions closely resembled the cation coordination by FSI⁻ anions. The anion coordination around cations in the liquid phase was significantly different from the ion packing observed in the crystal phase.

A smaller size of the FSI⁻ anion compared to that of the TFSI⁻ anion and a lower cation–anion binding energy were responsible for the faster transport in [emim][FSI] than in [emim][TFSI]. The smaller size of the emim⁺ cation compared to that of the pyr₁₃⁺ cation, the lower heat of vaporization of emim⁺-based IL compared to those in pyr₁₃⁺-based ILs, and the way the anion is distributed around the cations were suggested as the three primary reasons why ion transport in emim⁺-based ILs is faster compared to that in pyr₁₃⁺-based ILs. Analysis of the ion transport indicated that the FSI⁻ conformational relaxation was found to be decoupled from the ion translational motion, while the TFSI⁻ conformation dynamics showed some coupling with the ion transport. A slowing down of the TFSI⁻ conformational motion by 2 orders of magnitude reduced ion transport only by 40–50%.

Acknowledgment. We are grateful for financial support of this work by Air Force Office of Scientific Research, Department of the Air Force, contract number FA9550-09-C-0110 to Wasatch Molecular Inc. and the Department of Energy under

Contract Nos. DE-SC0001912 and DE-AC02-05CH11231 on PO No. 6838611 to University of Utah. Opinions, interpretations, conclusions, and recommendations are those of the authors and are not necessarily endorsed by the United States Air Force and DOE. An allocation of computer time from the Center for High Performance Computing at the University of Utah is gratefully acknowledged. We also would like to thank John Kerr and Wesley Henderson for numerous stimulating discussions.

Supporting Information Available: Apparent degree of ion uncorrelated motion, mean-square displacements, and their fits. This material is available free of charge via the Internet at <http://pubs.acs.org>.

References and Notes

- (1) Seki, S.; Kobayashi, Y.; Miyashiro, H.; Ohno, Y.; Usami, A.; Mita, Y.; Watanabe, M.; Terada, N. *Chem. Commun.* **2006**, 544–545.
- (2) Shin, J. H.; Henderson, W. A.; Passerini, S. *Electrochim. Commun.* **2003**, 5, 1016–1020.
- (3) Garcia, B.; Lavalée, S.; Perron, G.; Michot, C.; Armand, M. *Electrochim. Acta* **2004**, 49, 4583–4588.
- (4) Galinski, M.; Lewandowski, A.; Stepiak, I. *Electrochim. Acta* **2006**, 51, 5567–5580.
- (5) Alam, M. T.; Islam, M. M.; Okajima, T.; Ohsaka, T. *J. Phys. Chem. C* **2008**, 112, 16600–16608.
- (6) Aurbach, D.; Levi, M. D.; Salitra, G.; Levy, N.; Pollak, E.; Muthu, J. *J. Electrochem. Soc.* **2008**, 155, A745–A753.
- (7) Bao, Q. L.; Bao, S. J.; Li, C. M.; Qi, X.; Pan, C. X.; Zang, J. F.; Lu, Z. S.; Li, Y. B.; Tang, D. Y.; Zhang, S.; Lian, K. *J. Phys. Chem. C* **2008**, 112, 3612–3618.
- (8) Fedorov, M. V.; Kornyshev, A. A. *J. Phys. Chem. B* **2008**, 112, 11868–11872.
- (9) Fedorov, M. V.; Kornyshev, A. A. *Electrochim. Acta* **2008**, 6835–6840.
- (10) Huang, J. S.; Sumpter, B. G.; Meunier, V. *Angew. Chem.-Int. Ed.* **2008**, 47, 520–524.
- (11) Bai, Y.; Cao, Y. M.; Zhang, J.; Wang, M.; Li, R. Z.; Wang, P.; Zakeeruddin, S. M.; Gratzel, M. *Nat. Mater.* **2008**, 7, 626–630.
- (12) Forsyth, S. A.; Pringle, J. M.; MacFarlane, D. R. *Aust. J. Chem.* **2004**, 57, 113–119.
- (13) Ding, J.; Zhou, D.; Spinks, G.; Wallace, G.; Forsyth, S.; Forsyth, M.; MacFarlane, D. *Chem. Mater.* **2003**, 15, 2392–2398.
- (14) Huang, X. H.; Margulis, C. J.; Li, Y. H.; Berne, B. J. *J. Am. Chem. Soc.* **2005**, 127, 17842–17851.
- (15) Tokuda, H.; Tabata, S. I.; Susan, M. A. B. H.; Hayamizu, K.; Watanabe, M. *J. Phys. Chem. B* **2004**, 108, 11995–12002.
- (16) Tokuda, H.; Hayamizu, K.; Ishii, K.; Abu Bin Hasan Susan, M.; Watanabe, M. *J. Phys. Chem. B* **2004**, 108, 16593–16600.
- (17) Tokuda, H.; Hayamizu, K.; Ishii, K.; Susan, M. A. B. H.; Watanabe, M. *J. Phys. Chem. B* **2005**, 109, 6103–6110.
- (18) Borodin, O. *J. Phys. Chem. B* **2009**, 113, 12353–12357.
- (19) Matsumoto, H.; Sakaue, H.; Tatsumi, K.; Kikuta, M.; Ishiko, E.; Kono, M. *J. Power Sources* **2006**, 160, 1308–1313.
- (20) Wang, Y. D.; Zaghib, K.; Guerfi, A.; Bazito, F. F. C.; Torresi, R. M.; Dahn, J. R. *Electrochim. Acta* **2007**, 52, 6346–6352.
- (21) Kobayashi, Y.; Mita, Y.; Seki, S.; Ohno, Y.; Miyashiro, H.; Terada, N. *J. Electrochim. Soc.* **2007**, 154, A677–A681.
- (22) Zhou, Q.; Henderson, W. A.; Appetecchi, G. B.; Montanino, M.; Passerini, S. *J. Phys. Chem. B* **2008**, 112, 13577–13580.
- (23) Fujii, K.; Seki, S.; Fukuda, S.; Takamuku, T.; Kohara, S.; Kameda, Y.; Umebayashi, Y.; Ishiguro, S. *J. Mol. Liq.* **2008**, 143, 64–69.
- (24) Guerfi, A.; Duchesne, S.; Kobayashi, Y.; Vlijh, A.; Zaghib, K. *J. Power Sources* **2008**, 175, 866–873.
- (25) Pringle, J. M.; Golding, J.; Baranyai, K.; Forsyth, C. M.; Deacon, G. B.; Scott, J. L.; MacFarlane, D. R. *New J. Chem.* **2003**, 27, 1504–1510.
- (26) MacFarlane, D. R.; Meakin, P.; Sun, J.; Amini, N.; Forsyth, M. *J. Phys. Chem. B* **1999**, 103, 4164–4170.
- (27) Seki, S.; Kobayashi, Y.; Miyashiro, H.; Ohno, Y.; Usami, A.; Mita, Y.; Kihira, N.; Watanabe, M.; Terada, N. *J. Phys. Chem. B* **2006**, 110, 10228–10230.
- (28) Nicotera, I.; Oliviero, C.; Henderson, W. A.; Appetecchi, G. B.; Passerini, S. *J. Phys. Chem. B* **2005**, 109, 22814–22819.
- (29) Henderson, W. A.; Passerini, S. *Chem. Mater.* **2004**, 16, 2881–2885.
- (30) Borodin, O.; Smith, G. D. *J. Phys. Chem. B* **2006**, 110, 11481–11490.
- (31) Borodin, O.; Smith, G. D.; Henderson, W. J. *Phys. Chem. B* **2006**, 110, 16879–16886.
- (32) Borodin, O. *J. Phys. Chem. B* **2009**, 113, 11463–11478.
- (33) Borodin, O.; Smith, G. D.; Kim, H. *J. Phys. Chem. B* **2009**, 113, 4771–4774.
- (34) Smith, G. D.; Borodin, O.; Li, L.; Kim, H.; Liu, Q.; Bara, J. E.; Gin, D. L.; Nobel, R. *Phys. Chem. Chem. Phys.* **2008**, 10, 6301–6312.
- (35) Borodin, O. In *Molecular Dynamics Simulations of Ionic Liquids: Influence of Polarization on IL Structure and Ion Transport*, Materials Research Society Spring Meeting, San Francisco, 2008; Baker, G. A., Wilkes, J. S., Yang, H., Eds.; MRS: San Francisco, 2008; pp Q06–04.
- (36) Borodin, O.; Smith, G. D. *J. Phys. Chem. B* **2009**, 113, 1763–1776.
- (37) Canongia Lopes, J. N.; Padua, A. A. H.; Shimizu, K. *J. Phys. Chem. B* **2008**, 112, 5039–5046.
- (38) Padua, J. N. C.; Shimizu, K.; Padua, A. A. H.; Umebayashi, Y.; Fukuda, S.; Fujii, K.; Ishiguro, S. *J. J. Phys. Chem. B* **2008**, 112, 1465–1472.
- (39) Canongia Lopes, J. N.; Deschamps, J.; Padua, A. A. H. *J. Phys. Chem. B* **2004**, 108, 2038–2047.
- (40) Canongia Lopes, J. N.; Deschamps, J.; Padua, A. A. H. In *Ionic Liquids IIIa: Fundamentals, Progress, Challenges, and Opportunities, Properties and Structure*; Rogers, R. D., Seddon, K. R., Eds. Oxford University Press: 2005; pp 134–149.
- (41) Canongia Lopes, J. N.; Padua, A. A. H. *J. Phys. Chem. B* **2004**, 108, 16893–16898.
- (42) Deschamps, J.; Padua, A. A. H. In *Ionic Liquids IIIa: Fundamentals, Progress, Challenges, and Opportunities, Properties and Structure*; Rogers, R. D., Seddon, K. R., Eds. Oxford University Press: 2005; pp 150–158.
- (43) Canongia Lopes, J. N. A.; Padua, A. A. H. *J. Phys. Chem. B* **2006**, 110, 3330–3335.
- (44) Wu, X. P.; Liu, Z. P.; Wang, W. C. *Acta Phys.-Chim. Sinica* **2005**, 21, 1138–1142.
- (45) Canongia Lopes, J. N. A.; Padua, A. A. H. *J. Phys. Chem. B* **2006**, 110, 7485–7489.
- (46) Deetlefs, M.; Hardacre, C.; Nieuwenhuizen, M.; Padua, A. A. H.; Sheppard, O.; Soper, A. K. *J. Phys. Chem. B* **2006**, 110, 12055–12061.
- (47) Canongia Lopes, J. N.; CostaGomes, M. F.; Padua, A. A. H. *J. Phys. Chem. B* **2006**, 110, 16816–16818.
- (48) Canongia Lopes, J. N.; Padua, A. A. H. *J. Phys. Chem. B* **2006**, 110, 19586–19592.
- (49) Bagno, A.; D'Amico, F.; Saielli, G. *J. Mol. Liq.* **2007**, 131, 17–23.
- (50) Canongia Lopes, J. N.; Shimizu, K.; Padua, A. A. H.; Umebayashi, Y.; Fukuda, S.; Fujii, K.; Ishiguro, S. *J. Phys. Chem. B* **2008**, 112, 9449–9455.
- (51) Shah, J. K.; Maginn, E. J. *J. Phys. Chem. B* **2005**, 109, 10395–10405.
- (52) Cadena, C.; Zhao, Q.; Snurr, R. Q.; Maginn, E. J. *J. Phys. Chem. B* **2006**, 110, 2821–2832.
- (53) Morrow, T. I.; Maginn, E. J. *J. Phys. Chem. B* **2002**, 106, 12807–12813.
- (54) Shah, J. K.; Brennecke, J. F.; Maginn, E. J. *Green Chem.* **2002**, 4, 112–118.
- (55) Cadena, C.; Maginn, E. J. *J. Phys. Chem. B* **2006**, 110, 18026–18039.
- (56) Kelkar, M. S.; Maginn, E. J. *J. Phys. Chem. B* **2007**, 111, 4867–4876.
- (57) Kelkar, M. S.; Maginn, E. J. *J. Phys. Chem. B* **2007**, 111, 9424–9427.
- (58) Maginn, E. J. *Acc. Chem. Res.* **2007**, 40, 1200–1207.
- (59) Jayaraman, S.; Maginn, E. J. *J. Chem. Phys.* **2007**, 127, 214504.
- (60) Shi, W.; Maginn, E. J. *J. Phys. Chem. B* **2008**, 112, 2045–2055.
- (61) Koddermann, T.; Paschek, D.; Ludwig, R. *Chemphyschem* **2007**, 8, 2464–2470.
- (62) Sambasivaran, S. V.; Acevedo, O. *J. Chem. Theory Comput.* **2009**, 5, 1038–1050.
- (63) Fukuda, S.; Takeuchi, M.; Fujii, K.; Kanzaki, R.; Takamuku, T.; Chiba, K.; Yamamoto, H.; Umebayashi, Y.; Ishiguro, S. *J. Mol. Liq.* **2008**, 143, 2–7.
- (64) Tsuzuki, S.; Shinoda, W.; Saito, H.; Mikami, M.; Tokuda, H.; Watanabe, M. *J. Phys. Chem. B* **2009**, 113, 10641–10649.
- (65) Zhao, W.; Leroy, F.; Heggen, B.; Zahn, S.; Kirchner, B.; Balasubramanian, S.; Muller-Plathe, F. *J. Am. Chem. Soc.* **2009**, 131, 15825–15833.
- (66) Monteiro, M. J.; Bazito, F. F. C.; Siqueira, L. J. A.; Ribeiro, M. C. C.; Torresi, R. M. *J. Phys. Chem. B* **2008**, 112, 2102–2109.
- (67) Yan, T. Y.; Burnham, C. J.; Del Popolo, M. G.; Voth, G. A. *J. Phys. Chem. B* **2004**, 108, 11877–11881.
- (68) Chang, T. M.; Dang, L. X. *J. Phys. Chem. A* **2009**, 113, 2127–2135.
- (69) Santos, L. M. N. B. F.; Canongia Lopes, J. N.; Coutinho, J. A. P.; Esperanca, J. M. S. S.; Gomes, L. R.; Marrucho, I. M.; Rebelo, L. P. N. *J. Am. Chem. Soc.* **2007**, 129, 284–285.
- (70) Picalek, J.; Kolafa, J. *J. Mol. Liq.* **2007**, 134, 29–33.
- (71) Micaelo, N. M.; Baptista, A. M.; Soares, C. M. *J. Phys. Chem. B* **2006**, 110, 14444–14451.

- (72) Wei, Z.; Leroy, F.; Balasubramanian, S.; Muller-Plathe, F. *J. Phys. Chem. B* **2008**, *112*, 8129–8133.
- (73) Koddermann, T.; Paschek, D.; Ludwig, R. *Chemphyschem* **2008**, *9*, 549–555.
- (74) Koddermann, T.; Ludwig, R.; Paschek, D. *Chemphyschem* **2008**, *9*, 1851–1858.
- (75) Fujii, K.; Soejima, Y.; Kyoshino, Y.; Fukuda, S.; Kanzaki, R.; Umebayashi, Y.; Yamaguchi, T.; Ishiguro, S. I.; Takamuku, T. *J. Phys. Chem. B* **2008**, *112*, 4329–4336.
- (76) Fujii, K.; Fujimori, T.; Takamuku, T.; Kanzaki, R.; Umebayashi, Y.; Ishiguro, S. I. *J. Phys. Chem. B* **2006**, *110*, 8179–8183.
- (77) Umebayashi, Y.; Mitsugi, T.; Fukuda, S.; Fujimori, T.; Fujii, K.; Kanzaki, R.; Takeuchi, M.; Ishiguro, S. I. *J. Phys. Chem. B* **2007**, *111*, 13028–13032.
- (78) Umebayashi, Y.; Yamaguchi, T.; Fukuda, S.; Mitsugi, T.; Takeuchi, M.; Fujii, K.; Ishiguro, S. *Anal. Sci.* **2008**, *24*, 1297–1304.
- (79) Gorecki, W.; Jeannin, M.; Belorizky, E.; Roux, C.; Armand, M. *J. Phys.: Condens. Matter* **1995**, 6823.
- (80) Pierce, F.; Tsige, M.; Borodin, O.; Perahia, D.; Grest, G. S. *J. Chem. Phys.* **2008**, *128*, 214903–14.
- (81) Borodin, O.; Smith, G. D.; Sewell, T. D.; Bedrov, D. *J. Phys. Chem. B* **2008**, *112*, 734–742.
- (82) Borodin, O.; Smith, G. D. *J. Phys. Chem. B* **2006**, *110*, 6279–6292.
- (83) Borodin, O.; Smith, G. D. *J. Phys. Chem. B* **2006**, *110*, 6293–6299.
- (84) Borodin, O.; Smith, G. D. *J. Phys. Chem. B* **2003**, *107*, 6801–6812.
- (85) Borodin, O.; Smith, G. D.; Douglas, R. *J. Phys. Chem. B* **2003**, *107*, 6824–6837.
- (86) Borodin, O.; Smith, G. D. *J. Phys. Chem. B* **2006**, *110*, 4971–4977.
- (87) Borodin, O.; Smith, G. D. *Macromolecules* **2006**, *39*, 1620–1629.
- (88) Borodin, O.; Smith, G. D.; Fan, P. *J. Phys. Chem. B* **2006**, *110*, 22773–22779.
- (89) Ayyagari, C.; Bedrov, D.; Borodin, O.; Smith, G. D. *Lucretius*, M. D. Simulation code <http://www.eng.utah.edu/~gdsmit/lucratus.html>.
- (90) Dunweg, B.; Kremer, K. *J. Chem. Phys.* **1993**, *99*, 6983–6997.
- (91) Frenkel, D.; Smit, B. *Understanding Molecular Simulation: From Algorithms to Applications*, 2nd ed.; Academic Press: New York, 2002.
- (92) Mondello, M.; Grest, G. S. *J. Chem. Phys.* **1997**, *106*, 9327–9336.
- (93) Tokuda, H.; Ishii, K.; Susan, M. A. B. H.; Tsuzuki, S.; Hayamizu, K.; Watanabe, M. *J. Phys. Chem. B* **2006**, *110*, 2833–2839.
- (94) Kikuta, M.; Kono, M.; Ishikawa, M. *ECS Meeting Abstracts* **2008**, *802*, 615.
- (95) Fujii, K.; Seki, S.; Fukuda, S.; Kanzaki, R.; Takamuku, T.; Umebayashi, Y.; Ishiguro, S. *J. Phys. Chem. B* **2007**, *111*, 12829–12833.
- (96) Umebayashi, Y.; Mitsugi, T.; Fujii, K.; Seki, S.; Chiba, K.; Yamamoto, H.; Canongia Lopes, J. N.; Padua, A. A. H.; Takeuchi, M.; Kanzaki, R.; Ishiguro, S. *J. Phys. Chem. B* **2009**, *113*, 4338–4346.
- (97) Boyd, R. H.; Gee, R. H.; Han, J.; Jin, Y. *J. Chem. Phys.* **1994**, *101*, 788–797.
- (98) Henderson, W. A. Private communication, 2009.

JP911950Q